

## SHORT-WAVE INSTABILITIES ON A VORTEX PAIR OF UNEQUAL STRENGTH CIRCULATION RATIO

Joine SO, Kris RYAN and Gregory J. SHEARD

Fluids Laboratory for Aeronautical and Industrial Research (FLAIR)  
Department of Mechanical Engineering,  
Monash University, Australia.

### ABSTRACT

The creation of vortex pairs occurs in a range of industries, including mixing, transport, and plastic moulding. In particular, vortex pairs are observed in the wake of aircraft, and are the cause of a significant hazard in the aviation industry. Instabilities, which grow on vortex pairs, have been shown to lead to rapid diffusion, thus limiting this safety concern. To date research has only considered instabilities growing on a vortex pair where each vortex has the same magnitude of circulation. However in practice it is unusual to have an equal strength vortex pair.

This investigation is the first to consider the instability modes that may develop on a Lamb-Oseen vortex pair of arbitrary circulation ratio. We find a significant change in the growth rates of all instability modes reported previously for an equal strength vortex pair. All simulations employ an accurate spectral-element method to discretise the domain coupled with a three-step time splitting scheme. A wide range of instability wavelengths is considered to ensure that all instability modes are captured. By identifying and enhancing the leading instability modes, we are able to enhance the dissipation of the vortex pair.

### NOMENCLATURE

$a$	characteristic vortex radius
$b$	vortex separation distance
$\omega_{axial}$	axial vorticity
$\Gamma_1$	circulation of weak vortex
$\Gamma_2$	circulation of strong vortex
$r$	radial dimension
$\nu$	kinematic viscosity
$\sigma$	instability mode growth rate
$\sigma^* = \sigma t_c$	normalized instability mode growth rate
$k$	instability mode wave number
$u, v, w$	velocity components
$p$	pressure
$t_c$	time normalization parameter

### INTRODUCTION

The stability of vortex pairs to linear perturbations have been the subject of intense study for several decades, due largely to the application of these findings in the enhanced dissipation of aircraft wakes, and an improvement in our understanding of turbulent vortex interactions (Jacquin *et al.* (2003)).

Much of this work has concentrated on perturbations growing on vortex pairs of equal magnitude circulation strength. Leweke and Williamson (1998) experimentally

considered an equal strength magnitude, counter-rotating vortex pair, finding two modes of instability, a large wavelength Crow (Crow (1970)) mode, and a small wavelength Kelvin (Kerswell (2002)) mode, growing on the vortex pair. They found that the interaction of the two instability modes substantially decreased the time for the vortex pair to dissipate.

By comparison with equal strength vortex pairs, relatively little work has considered vortex pairs of unequal circulation strength. Ortega *et al.* (2003) experimentally considered unequal-strength counter-rotating vortex pairs formed in the wake of a specific wing planform. The use of their specific wing planform restricted the range of circulation strength ratios they could consider. They observed several three-dimensional instability modes growing on the vortex cores, however little description of the modes was provided. Bristol *et al.* (2004), following the work of Crow (1970) and Crouch (1997), developed an analytical model to consider instabilities which may grow on a vortex pair of unequal strength circulation. However, the model was restricted to consider only large wavelength instabilities, and did not consider the effect that the vortex profile will have on the instability mode that could form. Comparing their results with Ortega *et al.* (2003), several discrepancies were noted, especially where instability modes had a short wavelength.

Many investigations (for example Le Dizes and Laporte (2002), Lacaze *et al.* (2007), or Kerswell (2002)) have considered the instabilities that may grow on a vortex pair by considering an isolated vortex immersed within a linear strain field, the strain field being carefully chosen such that it is equivalent to the presence of a nearby vortex. These investigations have identified a range of Kelvin modes that can promote enhanced dissipation. However, findings using this technique are limited, as the technique assumes that the strain field is vanishingly small. By contrast, So *et al.* (2009) has shown that unequal strength vortex pairs typically lead to high strain rates measured at the core of the weaker vortex. Coincidentally, it is the weaker vortex that we anticipate instabilities to grow preferentially.

In this study, we will consider several vortex pairs of unequal-strength counter-rotating vortices. Key to our investigation is to identify if the Kelvin modes identified in prior studies grow in our highly deformed vortex cores, or if new instability modes dominate the flow. These results will have direct application to the aviation field as unequal strength vortex clusters feature prominently in the wake of an aircraft.

## FLOW FIELD DESCRIPTION

In this study two counter-rotating Lamb-Oseen vortices, each of characteristic radius  $a$ , are placed a distance  $b$  apart as shown in figure 1. Initially, each vortex is defined in isolation with a Lamb-Oseen profile, defined as

$$\omega_{axial} = \frac{\Gamma}{\pi a_0^2} e^{-\left(\frac{r}{a_0}\right)^2} \quad (1)$$

where  $\Gamma$  is the circulation of the vortex,  $a_0$  is the initial vortex radius, and  $r$  is the radial dimension. For all simulations discussed here the length-scale ratio is initially set to  $a_0/b = 0.25$ . The circulation strength ratio may be defined as

$$\Lambda = \frac{\Gamma_1}{\Gamma_2} \quad (2)$$

where  $\Gamma_1$  is the circulation of the weaker vortex and  $\Gamma_2$  is the circulation of the stronger vortex. In this study we have restricted our attention to  $-0.1 \geq \Lambda \geq -1$ .

The effect of viscosity may be quantified through the Reynolds number, based on the circulation of the strongest vortex ( $Re = \Gamma_2/\nu$ ). Viscous effects act to increase the radius of each vortex core (see Le Dizès and Verga (2002) for details); this effect may be approximated to first order through the equation

$$a(t) = \sqrt{a_0^2 + 4\nu t} \quad (3)$$

For all simulations, the Reynolds number was set to 20000, to agree with the previous studies of Le Dizès and Laporte (2002), and to minimize the impact of viscous vortex radial growth. In addition, the initial core radii are equal for both vortices at the commencement of all simulations considered in this study. It should be noted that viscous forces will be more dominant in the vicinity of the weaker vortex, leading the core radius of the weak vortex to grow substantially more than the radius of the strong vortex at low  $|\Lambda|$ . The discrepancy in core radii is important as work by Le Dizès and Laporte (2002) and Lacaze *et al.* (2007), considering a single vortex immersed in a strain field, have shown that the instability wave-number,  $k$ , should be normalized by core radius. However, under the assumption that instabilities will grow preferentially in the weak vortex, it is this core radius that is most important. In this investigation we normalize  $k$  with the initial vortex core size  $a_0$ .

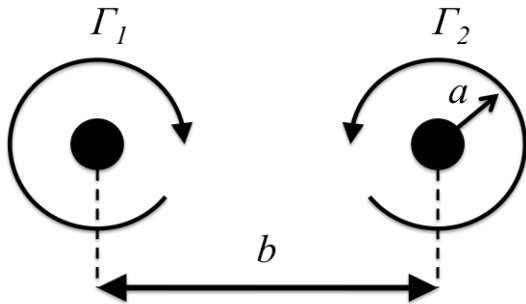


**Figure 1:** Schematic diagram of geometry.

## NUMERICAL TECHNIQUE

Two techniques are used to consider the problem. The first technique solves the two-dimensional incompressible Navier Stokes equations to evolve the base flow field such that the vortex pair adapt to a solution of Euler's equations. This relaxation process has been described in detail for equal strength vortex pairs by Le Dizès and Verga (2002) for co-rotating vortices, and Sipp *et al.* (2000) for counter-rotating vortices. More recently, So *et al.* (2009) has considered the case of  $|\Lambda| \neq 1$ . The base field is frozen at the conclusion of the relaxation process, to remove complexities introduced through viscous effects.

The growth-rate and mode-shape of linear perturbations acting on the relaxed vortex pair are then calculated through the solution of the linearized Navier-Stokes equations. This process assumes the perturbation velocity and pressure terms may be written in the general form

$$P' = \hat{P}(x, y) e^{ikz + i\sigma t}, \quad (4)$$

where  $P'$  represents any of the perturbation components ( $u', v', w'$  or  $p'$ );  $\hat{P}$  is the mode shape,  $k$  is the wave-number of the instability along the axis of the unperturbed vortex pair, and  $\sigma$  is the perturbation growth rate. In practice, a normalized growth rate,  $\sigma^* = \sigma t_c$ , is considered where

$$t_c = \frac{2\pi b^2}{|\Lambda| \Gamma_2}, \quad (5)$$

is the time taken for the strong vortex to travel a distance  $b$  along its path.

The general perturbation form of equation 4 is substituted into the linearized Navier-Stokes equations, leading to a sparse-matrix eigenvalue problem. The leading instability mode (defined as the mode with the largest growth rate) is calculated using an Arnoldi method as described by Sorensen (1995). Perturbation simulations are conducted in a rotating reference frame to match the rotation of the base field, where in general, the self-induced rotation rate of a vortex pair may be approximated as

$$\Omega = \frac{\Gamma_1 + \Gamma_2}{2\pi b^2}. \quad (6)$$

### Algorithm Employed

Spatial discretisation of the domain was achieved using a spectral-element technique, which, through the use of high-order interpolation polynomials, allowed highly accurate simulations (as described by Karniadakis *et al.* (1991)). A third-order time accurate technique was employed to model the solution of the Navier-Stokes equations (see Karniadakis *et al.* (1991)). This algorithm has been employed to solve similar problems previously, notably by Sheard *et al.* (2009) and Sheard and Ryan (2007).

The spatial accuracy was determined at run time by choosing the order of the tensor-product of interpolating polynomials within each macro-element as is usually possible with finite-element schemes. In all simulations quoted herein 441 macro-elements were employed. A square domain was considered with a domain length and width of 100 vortex diameters. The vortex pair was contained within a refined region at the centre of the mesh,

away from this region, the mesh density was reduced to limit computational expense.

## RESULTS

### The Two-Dimensional Relaxation Process

A flow field consisting of two circular vortices placed a finite distance apart is not a solution to the Navier-Stokes equations, and would not be observed experimentally. In order to generate an experimentally valid flow field numerically, the initial flow field is evolved in two-dimensions such that the solution relaxes to a solution of the Navier-Stokes equations. This relaxation process is driven by the strain rate within the core of each vortex evolving due to the external strain field generated by the other vortex, and is an inviscid process. The process has been described in detail for an unequal strength vortex pair by So *et al.* (2009).

Figure 2 shows contours of vorticity for the adapted vortex pair for several values of  $\Lambda$ . As  $\Lambda \rightarrow 0$ , the weaker vortex becomes increasingly deformed, and the profile of each vortex is increasingly different to that of the other vortex. Analytical investigations (for example Le Dizès and Laporte (2002)) of an isolated vortex in a strain field have shown that the magnitude of strain at the centre of a vortex is directly proportional to instability growth rate. Therefore, a-priori we may expect that for small  $\Lambda$ , instabilities will grow preferentially on the weaker vortex.

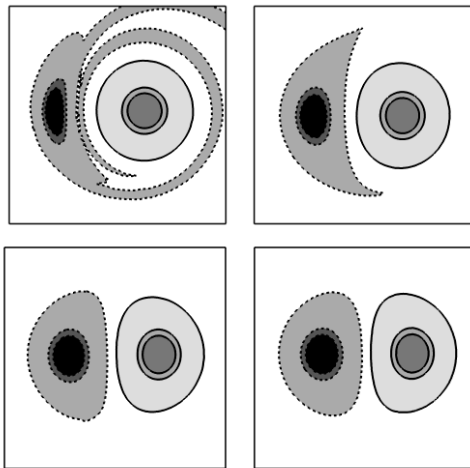


**Figure 2:** Vorticity contour snapshots for  $\Lambda = -0.1, -0.3, -0.7$  and  $-0.9$ . Snapshots show vorticity profiles after relaxation. Solid and dashed lines show positive and negative vorticity respectively.

$\Lambda$	$a_1/b$	$a_1/a_0$	$a_2/a_0$
-0.3	0.2677	1.0958	1.2860
-0.7	0.2731	1.1144	1.1544
-0.9	0.2748	1.1224	1.1317
-1.0	0.2761	1.1258	1.1258

**Table 1:** vortex core size at the conclusion of the adaptation phase, as a function of  $\Lambda$ .

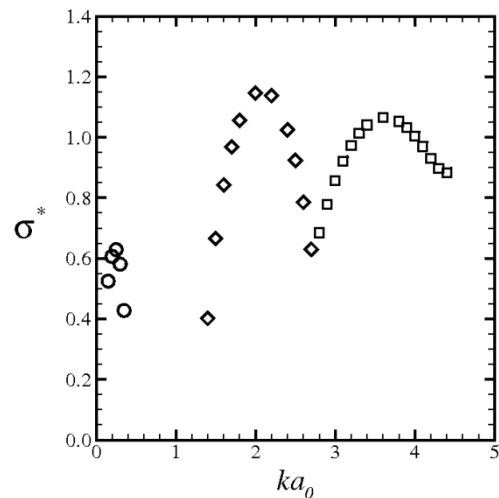
So *et al.* (2009) has shown that time required for the adaptation process to conclude is dependent on  $\Lambda$ . Table 1

details the core size of each vortex for selected values of  $\Lambda$  at the conclusion of the relaxation process. We note that as  $|\Lambda| \rightarrow 0$ , a discrepancy develops in the relative core sizes.

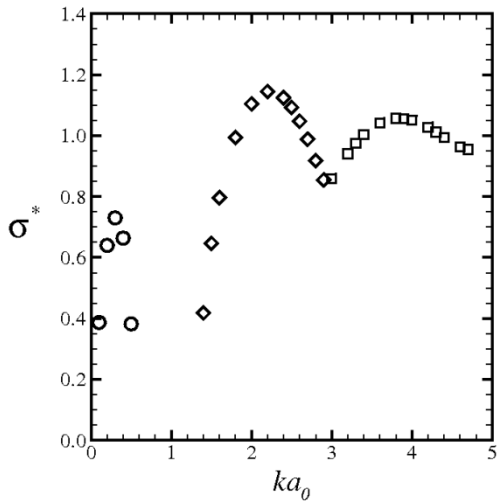
### Three-Dimensional Instability Growth Rates

Figure 3 shows the normalized growth rate,  $\sigma^* = \sigma \cdot t_c$ , of the leading instability mode as a function of the normalized wave-number,  $ka_0$ , for  $\Lambda = -0.9$ . This is the global growth rate, taking into account instability growth in the vicinity of both vortex cores. Three dominant instability modes have been identified. At low wave-numbers, the Crow instability is observed at  $ka_0 \approx 0.1$ , in close agreement with the analytical findings of Bristol *et al.* (2004). The normalized growth rate is slightly lower than their findings due to the effect of viscosity (not accounted for in their model).

Two further instability modes are also observed at higher wave-numbers, the first, with a peak at  $ka_0 = 2.1$ , is identified as the first solution branch of Kelvin mode  $(-1,1)$ . The second, with a peak at  $ka_0 = 3.55$ , is identified as the second solution branch of Kelvin mode  $(-1,1)$ . When comparing these results with Le Dizès and Laporte (2002), we find that both the peak growth rate for each mode, and the wave-number at which this occurs, agrees very well with the case of  $\Lambda = -1$ . Both modes have substantially higher growth rates than the Crow instability, and should dominate the flow experimentally.



**Figure 3:** Normalized instability growth rate as a function of axial wave-number for  $\Lambda = -0.9$ . Symbols indicate different mode-shapes;  $\circ$ , Crow instability;  $\diamond$  Kelvin mode  $(-1,1,1)$ ;  $\square$  Kelvin mode  $(-1,1,2)$ .



**Figure 4:** Normalized instability growth rate as a function of axial wave-number for  $\Lambda=-0.7$ . See figure 3 for symbol definitions.

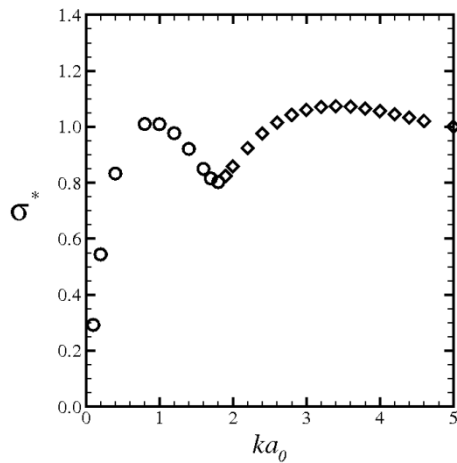


**Figure 5:** Normalized instability growth rate as a function of axial wave-number for  $\Lambda=-0.3$ . See figure 3 for symbol definitions.

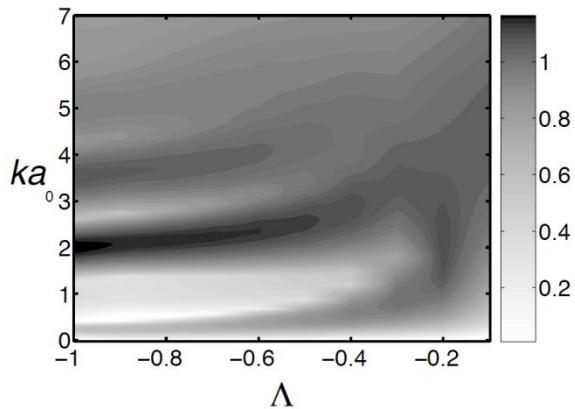
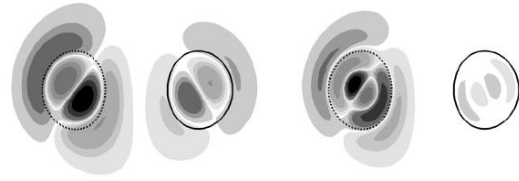
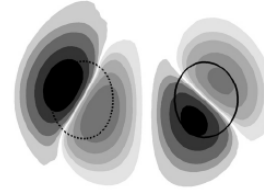


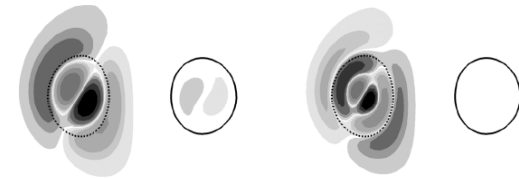
**Figure 6:** Contour map of normalized growth rate,  $\sigma^*$ , as a function of  $ka_0$  and  $\Lambda$ .



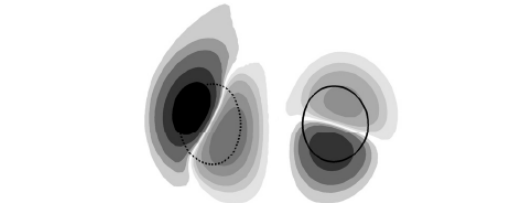
(a)  $\Lambda=-0.9$ . Mode  $(-1,1,1)$ .



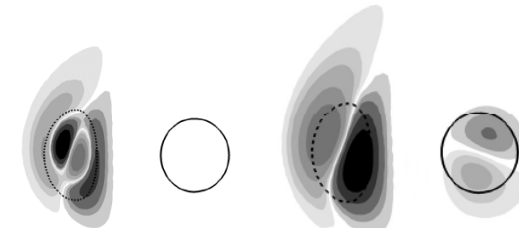
(b)  $\Lambda=-0.9$ . Mode  $(-1,1,2)$ .



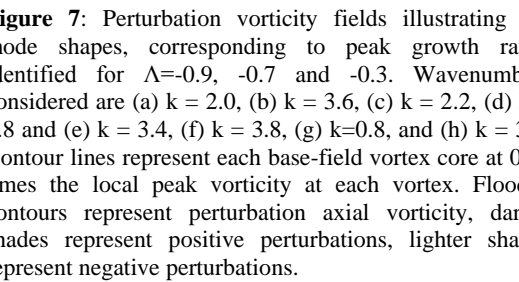
(c)  $\Lambda=-0.9$ . Crow instability mode.



(d)  $\Lambda=-0.7$ . Mode  $(-1,1,1)$ .



(e)  $\Lambda=-0.7$ . Mode  $(-1,1,2)$ .



(f)  $\Lambda=-0.7$ . Crow instability mode.

(g)  $\Lambda=-0.3$ . Mode  $(-1,1,1)$ .

(h)  $\Lambda=-0.3$ . Crow instability mode.

**Figure 7:** Perturbation vorticity fields illustrating the mode shapes, corresponding to peak growth rates, identified for  $\Lambda=-0.9$ ,  $-0.7$  and  $-0.3$ . Wavenumbers considered are (a)  $k = 2.0$ , (b)  $k = 3.6$ , (c)  $k = 2.2$ , (d)  $k = 3.8$  and (e)  $k = 3.4$ , (f)  $k = 3.8$ , (g)  $k=0.8$ , and (h)  $k = 3.4$ . Contour lines represent each base-field vortex core at 0.33 times the local peak vorticity at each vortex. Flooded contours represent perturbation axial vorticity, darker shades represent positive perturbations, lighter shades represent negative perturbations.

Figure 4 shows the instability growth rates for  $\Lambda = -0.7$ . All three modes identified for  $\Lambda = -0.9$  are observed once again. The Crow instability is found to have a higher

growth rate, and a peak growth rate at a higher wave-number, in agreement with the findings of Bristol *et al.* (2004). The Kelvin mode instabilities are also observed to have peak growth rates occurring at higher wave-numbers when compared with  $\Lambda = -0.9$ . However, the peak growth rates for both Kelvin modes are reduced when compared with  $\Lambda = -0.9$ . This trend is continued as the circulation strength ratio magnitude is further reduced to  $\Lambda = -0.3$  (figure 5). In this case, only the Crow instability and the first branch of the Kelvin mode  $(-1,1)$  are observed across the range of wave-numbers considered. Here, the Crow instability peak growth rate has increased to the point where it is comparable to that of the Kelvin mode instability. The range of wave-numbers over which the Kelvin mode has a significant growth rate is observed to be much broader than that observed at higher magnitudes of  $\Lambda$ .

Figure 6 shows a contour map of normalized instability growth rate as a function of  $\Lambda$  and  $ka_0$ . Dark bands represent local peaks in  $\sigma^*$ , each band representing a different mode of instability. All Kelvin instability modes are observed to reduce in strength as  $\Lambda \rightarrow 0$ , and are observed to have an increase in normalized wave-number. This is counter-intuitive, as the core radii of the weak vortex is greater as  $|\Lambda| \rightarrow 0$ . Therefore it is concluded that the increase in normalized mode wave-number as  $|\Lambda| \rightarrow 0$  is due to the increasing deformation of the weak vortex profile as observed in figure 2. By contrast, the long wavelength, Crow instability displays an increase in growth rate as  $\Lambda$  decreases, reaching a peak at  $\Lambda \approx -0.2$ . In line with the short wave-length Kelvin modes, the Crow instability also exhibits an increase in normalized wave number with decreasing  $\Lambda$ . When  $\Lambda \approx -0.2$ , the Crow instability is noted to share the same normalized wave number as the first branch solution of Kelvin mode  $(-1,1)$ . Below  $\Lambda \approx -0.2$  only one instability mode solution is observed to occur.

The mode shapes for each instability, calculated at the normalized wave-number corresponding to maximum growth, are shown in figure 7. The flooded contour images have been generated by subtracting the axial perturbation vorticity field,  $\omega_z$ , measured at a plane along the vortex axis, from  $\omega_z$  measured on another plane placed a distance  $2\pi/ka_0$  away. This allows us to identify all the relevant mode structures from analysis of a two dimensional field.

Figure 7a,b and c shows the instability mode-shapes for  $\Lambda = -0.9$ . As both vortices have very similar circulation strengths, we would expect that the instability mode shapes be almost identical on each vortex. This is indeed the case for the Crow instability (figure 7c), which induces a sinuous oscillation along the axis of both vortices. The mode structure of the Crow instability is observed to occur on a scale larger than the vortex core, with a peak in  $\omega_z$  observed on the vortex core radius. The growth of the Crow instability is observed to be slightly reduced on the strong vortex. By contrast, the Kelvin modes show reduced growth in the strong vortex when compared with the weak vortex. This is especially apparent in the second solution branch of the Kelvin mode  $(-1,1)$ . It is postulated that the reduction in perturbation strength acting on the strong vortex is directly linked to the scales included in the instability mode-shape. The long wavelength Crow instability has a very simple structure with large scales in all three dimensions. By contrast the Kelvin modes have

smaller scale structures and are highly dependent on the profile of the base vortex.

The strain at the centre of the strong vortex decreases with  $|\Lambda|$ . Thus, for the case  $\Lambda = -0.7$ , the perturbations do not develop as vigorously on the strong vortex, when compared with the case of  $\Lambda = -0.9$ . Indeed, at  $\Lambda = -0.7$ , only the Crow mode develops any appreciable perturbations on the strong vortex. Comparing  $\Lambda = -0.7$  with  $\Lambda = -0.9$ , it is interesting to note that the mode-shapes in the weak vortex have not altered appreciably with  $\Lambda$ .

As  $|\Lambda|$  is further reduced to  $\Lambda = -0.3$ , only two instability modes are observed. Considering figure 6, we note that for  $|\Lambda| < 0.5$ , the normalized wave-number where the second solution branch of the Kelvin mode grows is identical to the normalized wave-number where the first solution branch of the Kelvin mode grows. Given the higher growth rate of the first solution branch of the Kelvin mode, it is not surprising that the second branch solution is not observed for  $\Lambda = -0.3$ . The mode structure for the first solution branch of the Kelvin mode only appears on the highly strained, weak vortex. The strain of the base field has appreciably altered the mode shape. This is also apparent for the Crow instability that also grows more strongly on the weak vortex in preference to the strong vortex.

A three-dimensional representation of the instability mode may be obtained by adding the perturbation field, magnified by an arbitrary factor, to the base field. An example of this is shown in figure 8, for the first branch solution of the Kelvin mode  $(-1,1)$ , for  $\Lambda = -0.9$ . The figure clearly identifies the sinuous oscillation induced by the instability mode acting along the axis of both vortices.

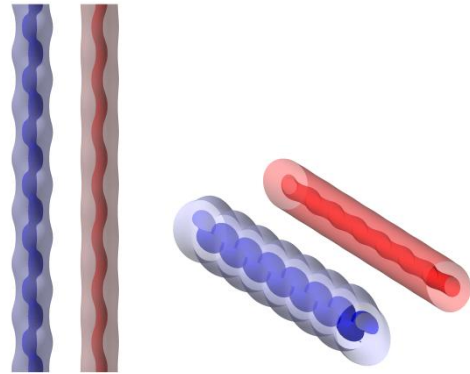


**Figure 8:** A three-dimensional representation of the instability mode  $(-1,1,1)$  for  $\Lambda = -0.9$ .

## DISCUSSION

Large wavelength Crow instabilities begin to dominate as  $|\Lambda| < 0.3$ . We note an increase in growth rate and critical wave-number for this mode for smaller  $|\Lambda|$ , in agreement with analytical findings of Bristol *et al.* (2003). Analytical evaluations of the Crow instability do not consider the effects of highly deformed core profile on the development of the mode. In line with their findings the severe deformation of the weak vortex noted for small  $|\Lambda|$  has little influence on the mode development.

By contrast, the growth of the short-wavelength Kelvin modes is highly dependent on the vortex profile. Slight deviations away from  $|\Lambda|=1$  results in a significant

asymmetry in instability mode development across the vortex cores. We note that even for  $\Lambda = -0.9$ , a significant difference is noted in the amplitude of the perturbation mode-shape growing on the weak vortex by comparison to the strong vortex. This is especially apparent for the second branch of mode  $(-1,1)$ , which has the most complicated structure.

In closing it should be stated that the linear instabilities observed do not any cause appreciable reduction in the coherence of either vortex core. However, they are the leading instability modes in a cascade that is expected to significantly increase the variation of the vortex pair along their axis. The linear perturbation mode-shape is critical to further non-linear instability developments. Enhanced dissipation of a vortex pair requires the development of instability modes on both vortex cores. In the absence of this, one vortex will remain coherent while the other is destroyed.

Further DNS investigations are required to elucidate the non-linear instability growth that occurs beyond the linear growth period, this work is continuing.

## CONCLUSION

Three instability modes have been identified across the range  $-1 < \Lambda < 0$ . These modes are equivalent to instability modes described in previous studies of equal strength counter-rotating vortex pairs. However, in this case, Kelvin mode instabilities are observed to grow preferentially on the weak vortex, and the global growth rate of these Kelvin modes reduces as  $|\Lambda| \rightarrow 0$ . By contrast the long wave-length Crow instability exhibits an increase in growth rate as  $|\Lambda|$  is reduced. In addition, the Crow instability exhibits strong growth on both vortex cores down to  $\Lambda = -0.3$ . These linear instability modes may lead to enhanced dissipation of the vortex pair.

## REFERENCES

- BRISTOL, R.L., ORTEGA, J.M., MARCUS, P.S. and SAVAS, O., (2004), "On cooperative instabilities of parallel vortex pairs", *J. Fluid Mech.* **517**, 331-358.
- CROW, S.C., (1970), "Stability theory for a pair of trailing vortices", *AIAA Journal*, **8**, 2172-2179.
- JACQUIN, L., FABRE, D., SIPP, D., THEOFOLIS, V and VOLLMERS, H., (2003), "Instability and unsteadiness of aircraft wake vortices", *Aerospace Science and Technology*, **7**, 577-593.
- KARNIADAKIS, G.E., ISRAELI, M., and ORSZAG, S.A. (1991) "High order splitting methods for the incompressible Navier-Stokes equations", *J. Comput Phys.*, **97**(2), 414-443.
- KERSWELL, R.R., (2002), "Elliptic instability", *Annu. Rev. Fluid Mech.*, **34**, 83-113.

LE DIZES, S. and LAPORTE F. (2002), "Theoretical predictions for the elliptic instability in a two-vortex flow", *J. Fluid Mech.* **471**, 169-201.

LE DIZES, S. and VERGA, A. (2002) "Viscous interactions of two co-rotating vortices before merging", *J. Fluid Mech.* **467**, 389-410.

LEWEKE, T. and WILLIAMSON, C.H.K., (1998), "Cooperative elliptic instability of a vortex pair", *J. Fluid Mech.* **360**, 85-119.

ORTEGA, J.M., BRISTOL, R.L., and SAVAS, O., (2004), "Experimental study of the instability of unequal-strength counter-rotating vortex pairs", *J. Fluid Mech.* **474**, 35-84.

SHEARD, G.J. and RYAN, K. (2007) "Pressure-driven flow past spheres moving in a circular tube." *J. Fluid Mech.* **592**, 233-262.

SHEARD, G.J., FITZGERALD, M.J., and RYAN, K. (2009) "Cylinders with square cross section: Wake instabilities with incidence angle variation." *J. Fluid Mech.* **630**, 43-69.

SIPP, D., JACQUIN, L. and COSSU, C. (2000) "Self-adaptation and viscous selection in concentrated two-dimensional dipoles", *Phys. Fluids*, **12** (2).

SO J., RYAN, K. and SHEARD, G.J., "Self-adaptation and relaxation of unequal-strength counter-rotating vortex pairs", (**Submitted**).

SORENSEN, D.C. (1995) "Implicitly restarted Arnoldi/Lanczos methods for large scale eigenvalue calculations", *Tech. Report TR-96-40*. In: KEYS, D.E., SAMEH, A., and VENKATKRISHNAN, V. (Eds), *Parallel numerical algorithms*. Dordrecht, Kluwer.